Supporting Information

Activating dynamic Zn-ZnO interface with controllable oxygen vacancy in CO_2 electroreduction for boosting CO production

Xueqi Liu,[a,#] Jingmin Ge,[a,#] Shiying Li,[b] Huanhuan Yang,[a,*] Huiwen Tian,[a] Hongpo Liu,[a] Yaxi Li,[a] Xiaoli Zheng,[a] Yapeng Tian,[a] Xinwei Cui,[a] and Qun Xu,[a,*]

[a] Henan Institute of Advanced Technology, Zhengzhou University, Zhengzhou 450002, China

[b] School of Mechanics and Safety Engineering, School of Materials Science and Engineering, Zhengzhou University, Zhengzhou 450001, China

[c] State Key Laboratory of Coal Conversion, Institute of Coal Chemistry, Chinese Academy of Sciences, Taiyuan 030001, China

[#] These authors contributed equally.

[*] Corresponding authors: yanghh@zzu.edu.cn (H. Yang); qunxu@zzu.edu.cn (Q. Xu)

Keywords:

Oxygen vacancies

Zn-ZnO interface

Electrochemical CO_2 reduction

Carbon monoxide

Dynamic evolution

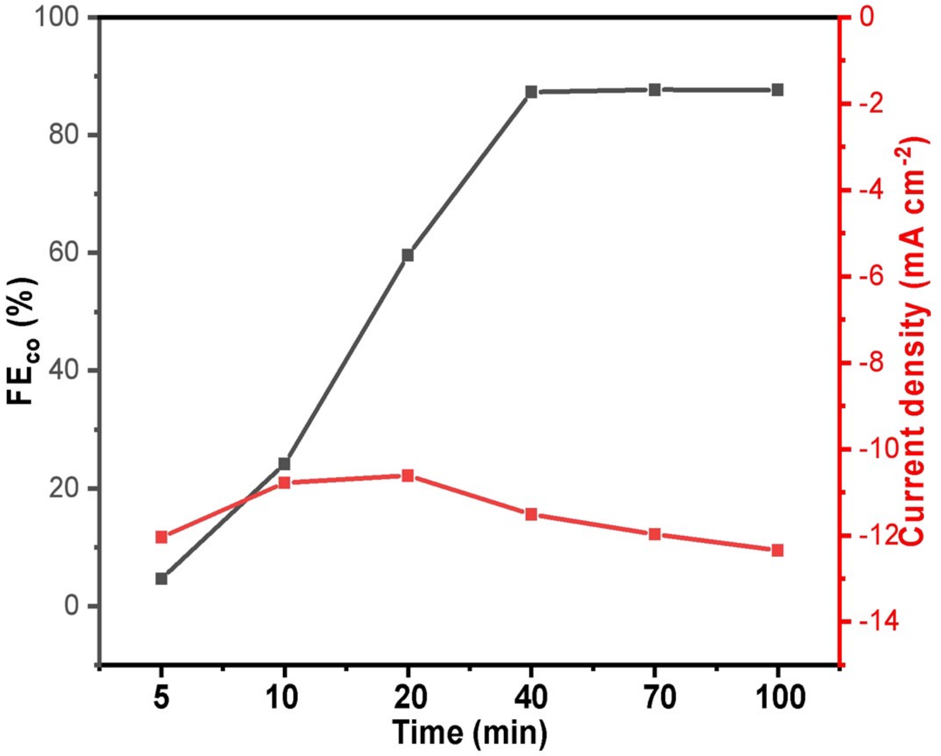

Figure S1. FE$_{CO}$ and the current density of ZnO-650 at −1.3 V (*vs.* RHE) in CO_2-saturated 0.1 M $KHCO_3$ at the initial 100 min.

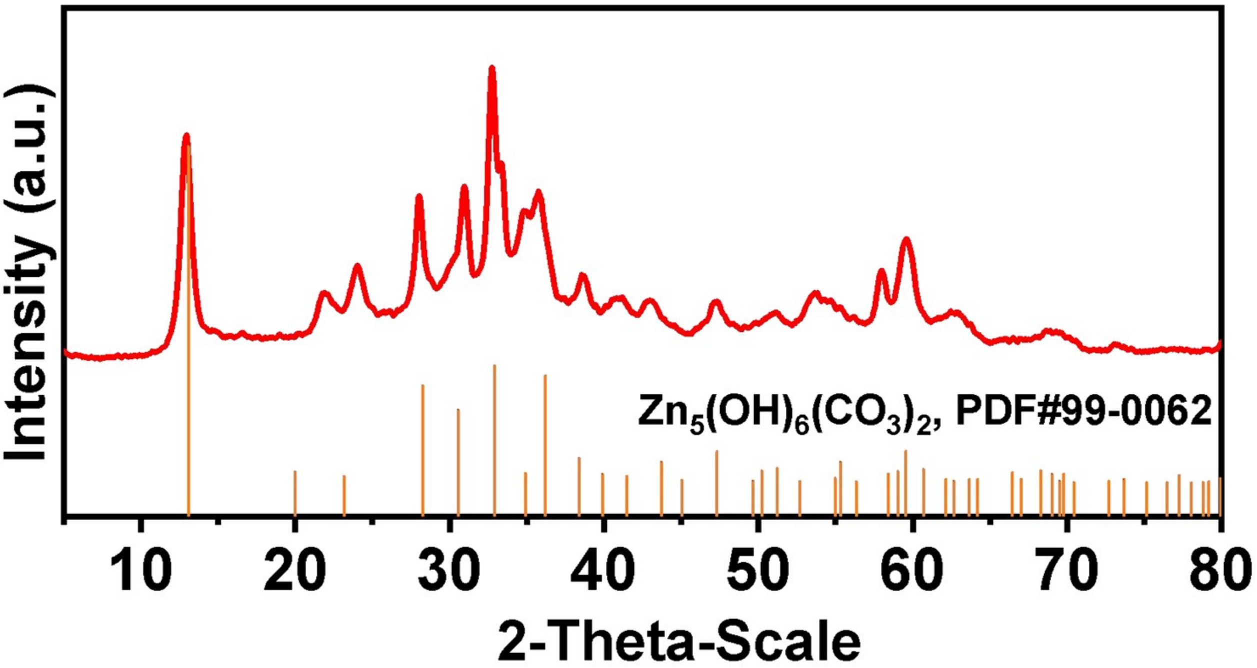

Figure S2. XRD pattern of the $Zn_5(OH)_6(CO_3)_2$ precursor.

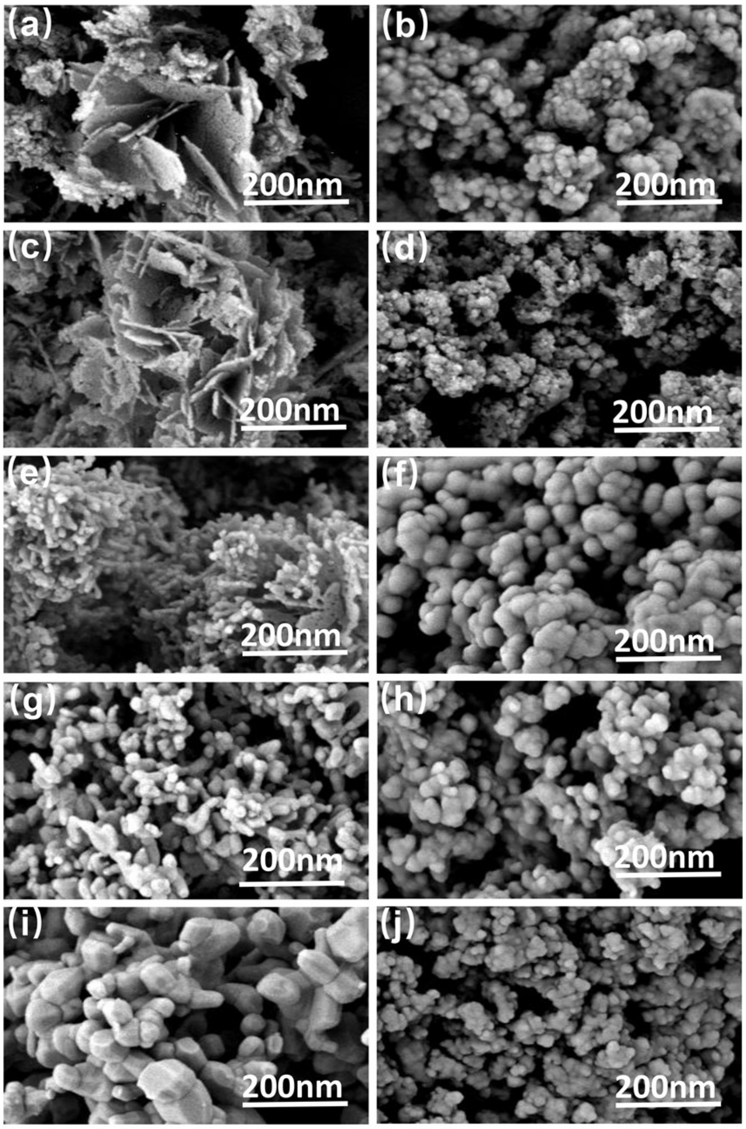

Figure S3. SEM images of (a) ZnO-200; (b) Zn@ZnO-200; (c) ZnO-350; (d) Zn@ZnO-350; (e) ZnO-500; (f) Zn@ZnO-500; (g) ZnO-650; (h) Zn@ZnO-650; (i) ZnO-800 and (j) Zn@ZnO-800.

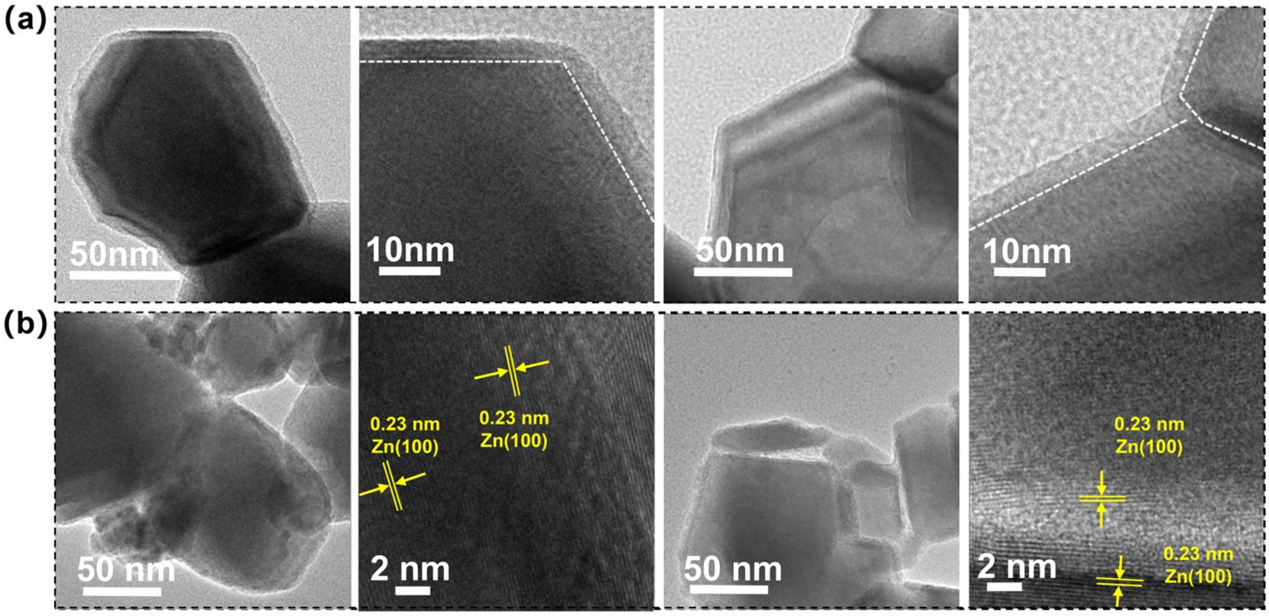

Figure S4. (a) (HR)TEM images of Zn@ZnO-650 taken after pre-treatment for 40 min at different regions; and (b) (HR) TEM images of Zn@ZnO-650 taken after pre-treatment for 10 min at different regions.

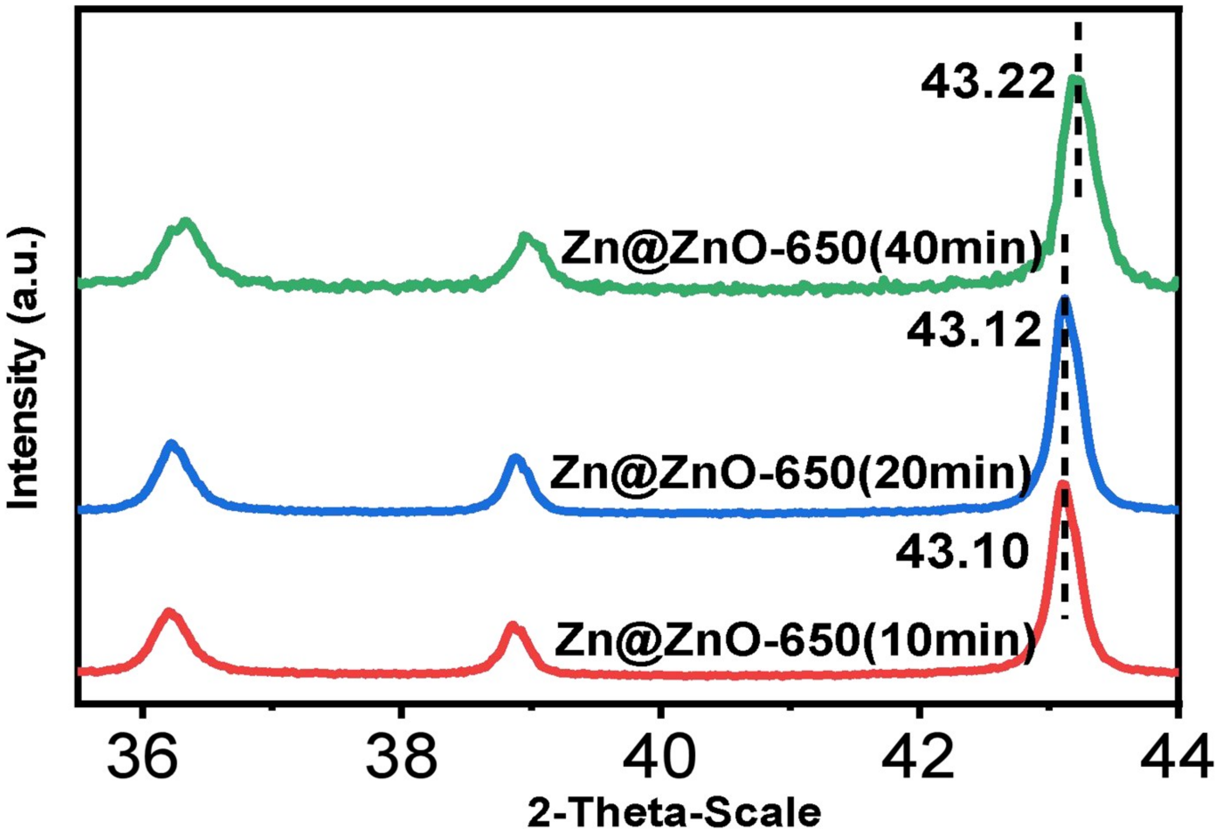

Figure S5. Enlarged XRD patterns at 2θ ranging from 35.5° to 44.0° of Zn@ZnO-650 with different pre-treatment time for 10, 20, 40 min.

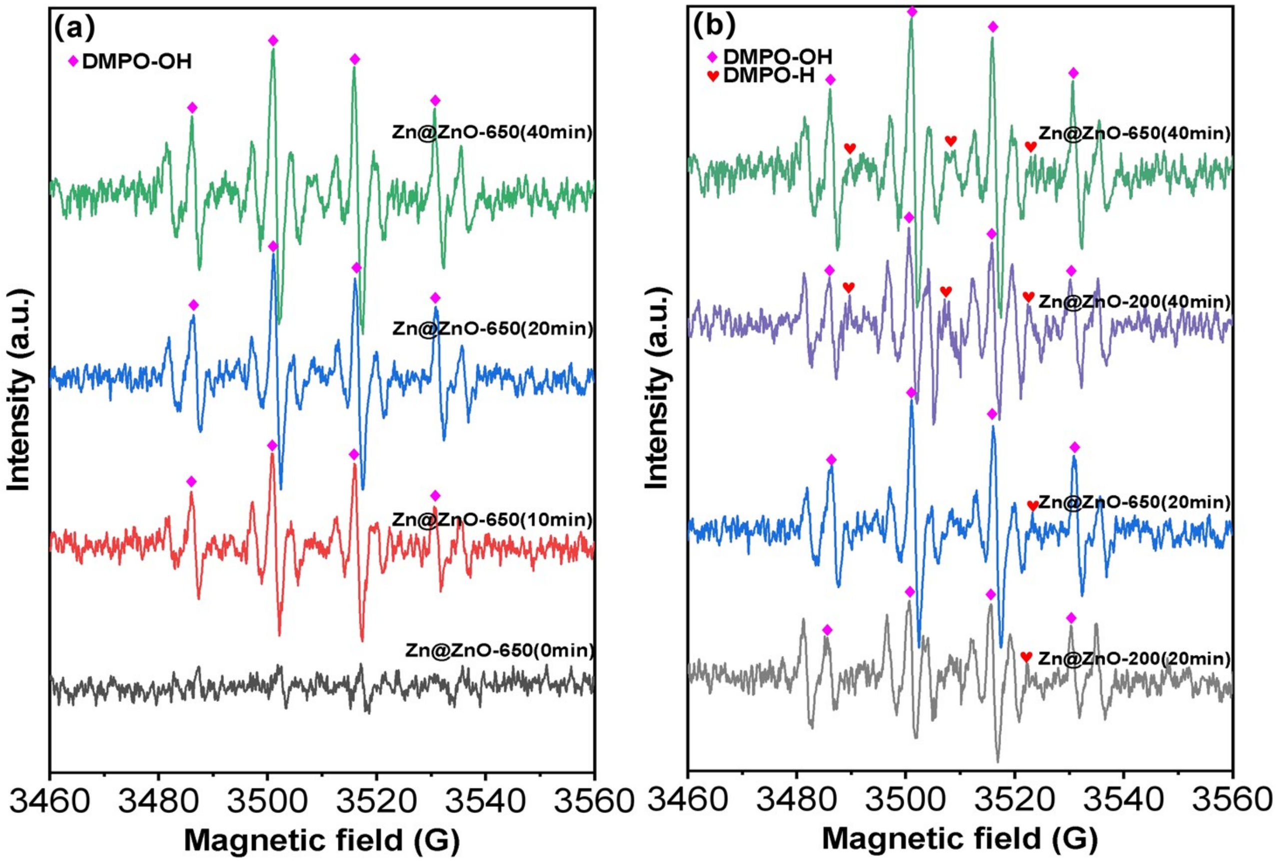

Figure S6. In situ EPR spectra of $OH^{\bullet-}$ were recorded in a CO_2-saturated 0.1 M $KHCO_3$ solution containing 100 mM DMPO for: (a) Zn@ZnO-650 with different pre-treatment time; and (b) comparison between Zn@ZnO-650 and Zn@ZnO-200.

It has been demonstrated that the oxide-derived metallic species during CO_2RR could be spontaneously re-oxidized due to the oxygen sources of inevitable dissolved oxygen or the formed oxidizing species like $OH^{\bullet-}$radicals in electrolyte[1]. Herein, 40 min of electrochemical pre-treatment of ZnO-650 and ZnO-200 at −1.3 V vs. RHE was performed in CO_2-saturated 0.1 M $KHCO_3$ solution containing 100 mM DMPO as spin trapping agent (5,5-Dimethyl-1-pyrroline N-oxide). As shown in Figure S6a, the signals of DMPO-OH gradually increased with the pre-treatment time till 40 min, suggesting a continuous production of $OH^{\bullet-}$. Taking ZnO-200 as a comparative sample (Figure S6b), the intensity of DMPO-OH signals at pre-treatment for 20 and 40 min were weakened, manifesting that less $OH^{\bullet-}$ formation in ZnO-200 system. More $OH^{\bullet-}$ generated in the pre-treatment process of ZnO-650 correspond to more abundant Zn-ZnO interface observed in TEM images, proving that $OH^{\bullet-}$ is the most likely oxidizing species that leads to the re-oxidation of Zn and the formation of the Zn−ZnO interface.

The reaction system and conditions of CO_2RR, including reactor, CO_2 flow rate, $KHCO_3$ electrolyte, applied potential and pre-treatment time, are same for all ZnO-*T* samples in this work. Thus, the effect of trace amount of oxygen in electrolyte on the re-oxidation of different ZnO-*T* derived Zn might be ignored. The difference of Zn-ZnO interface and oxygen vacancies in Zn@ZnO-*T* is most likely due to the re-oxidation of Zn by oxidizing $OH^{\bullet-}$ forming in electrolyte.

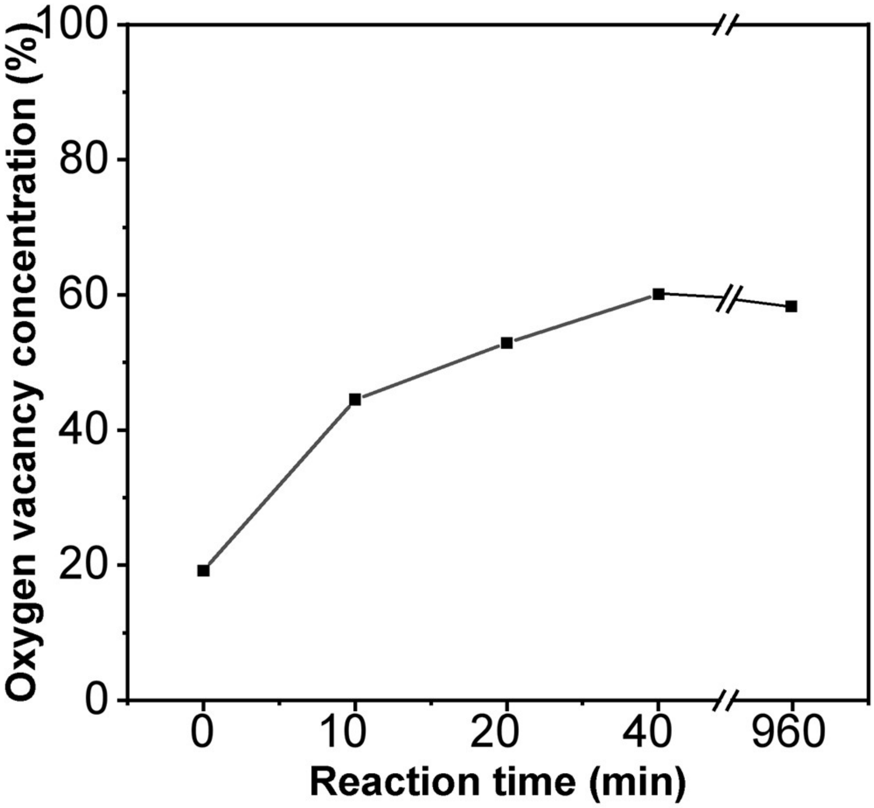

Figure S7. The relative concentrations of oxygen vacancies in Zn@ZnO-650 take after pre-treatment for different time at −1.3 V (*vs.* RHE) in CO_2-saturated 0.1 M $KHCO_3$. The data for 960 min calculated based on the O 1s XPS spectrum of Zn@ZnO-650 reaction at −1.2 V (*vs.* RHE) in CO_2-saturated 0.1 M $KHCO_3$ for 960 min.

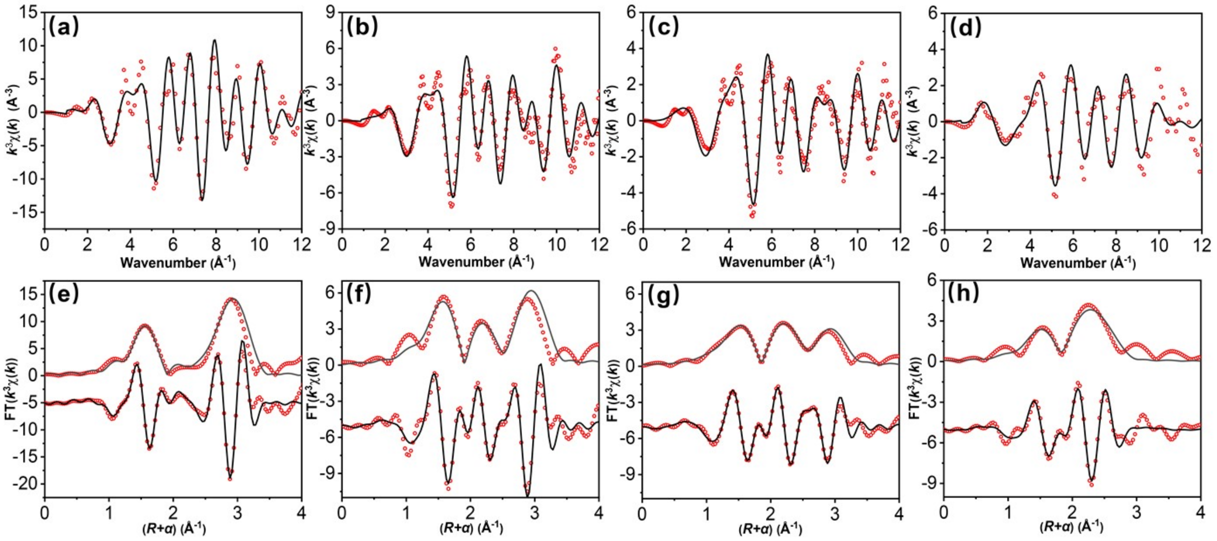

Figure S8. Experimental (points) and fitting (lines) Fourier transform Zn K-edge EXAFS spectra for (a) ZnO-650(0min), (b) Zn@ZnO-650(10min), (c) Zn@ZnO-650(20min) and (d) Zn@ZnO-650(40min), shown in k^3-weighted k-space; (e)ZnO-650(0min), (f) Zn@ZnO-650(10min), (g) Zn@ZnO-650(20min) and (h) Zn@ZnO-650(40min), shown in k^3-weighted R-space. All of the Fourier transform EXAFS data for the k^3-weighted are plotted without phase correction.

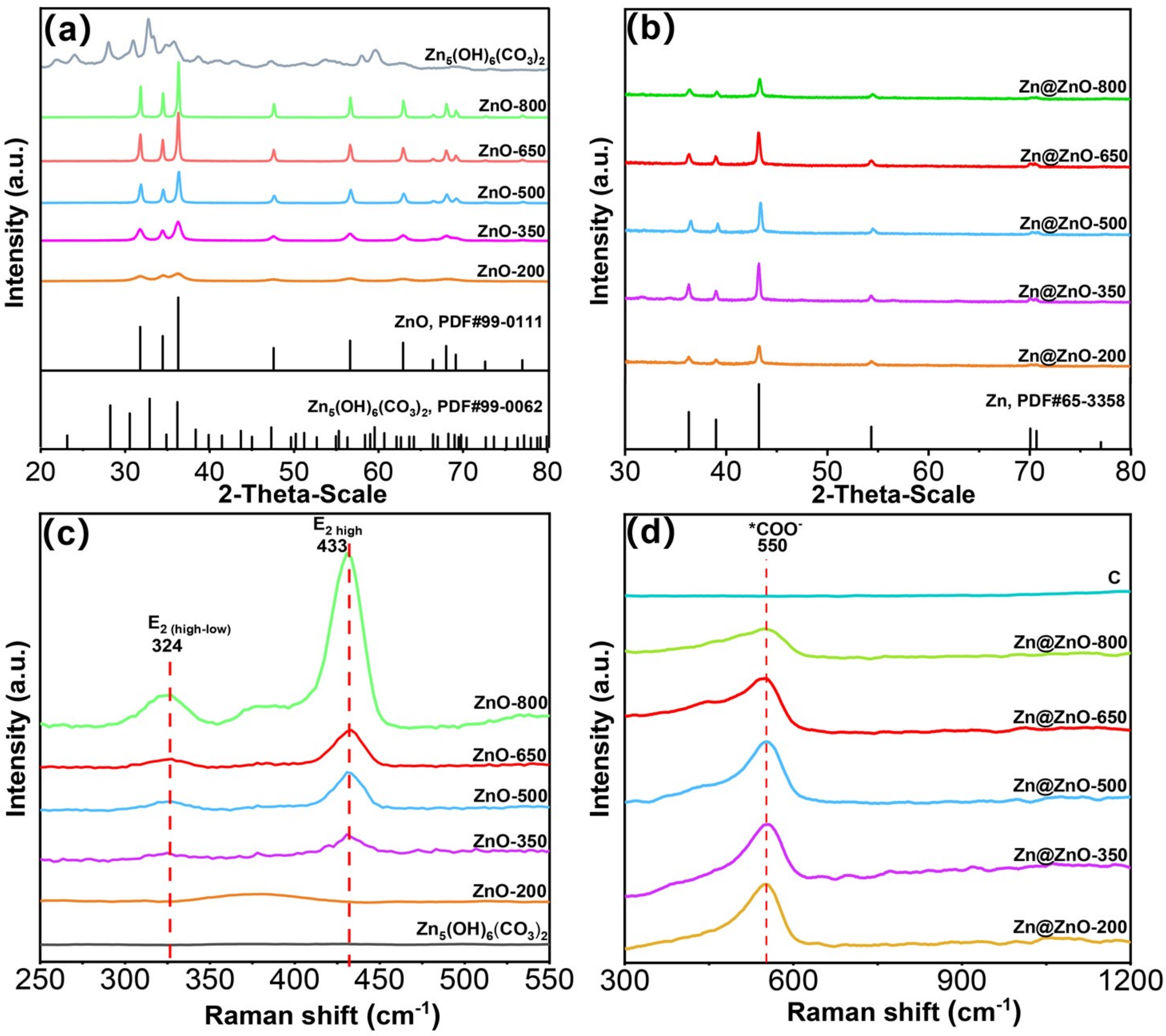

Figure S9. XRD patterns of (a) $Zn_5(OH)_6(CO_3)_2$, ZnO-*T* and (b) Zn@ZnO-*T*; Roman spectra of (c) $Zn_5(OH)_6(CO_3)_2$, ZnO-*T* and (d) Zn@ZnO-*T*.

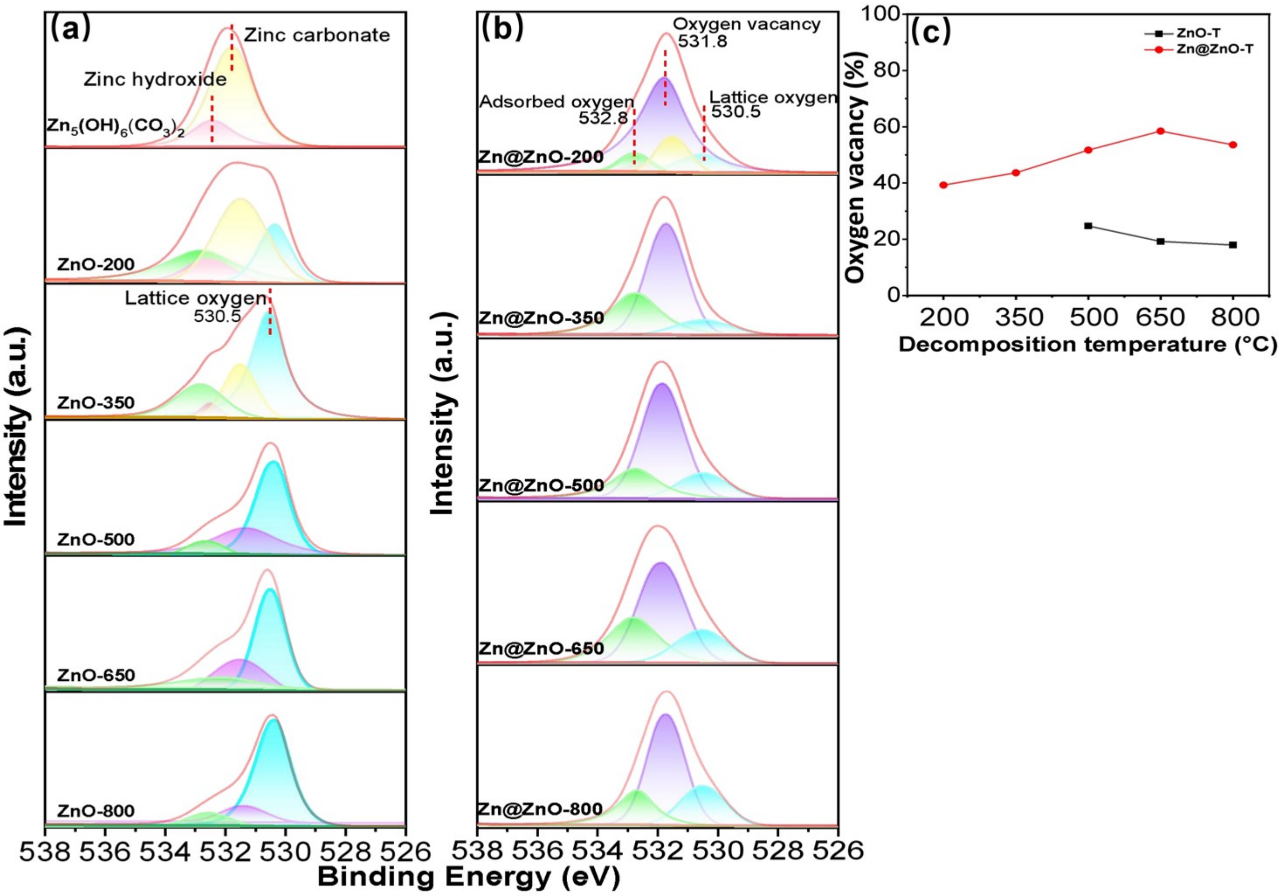

Figure S10. O 1s XPS spectra of (a) $Zn_5(OH)_6(CO_3)_2$, ZnO-*T* and (b) Zn@ZnO-*T*; (c) Relative concentrations of oxygen vacancies for different samples.

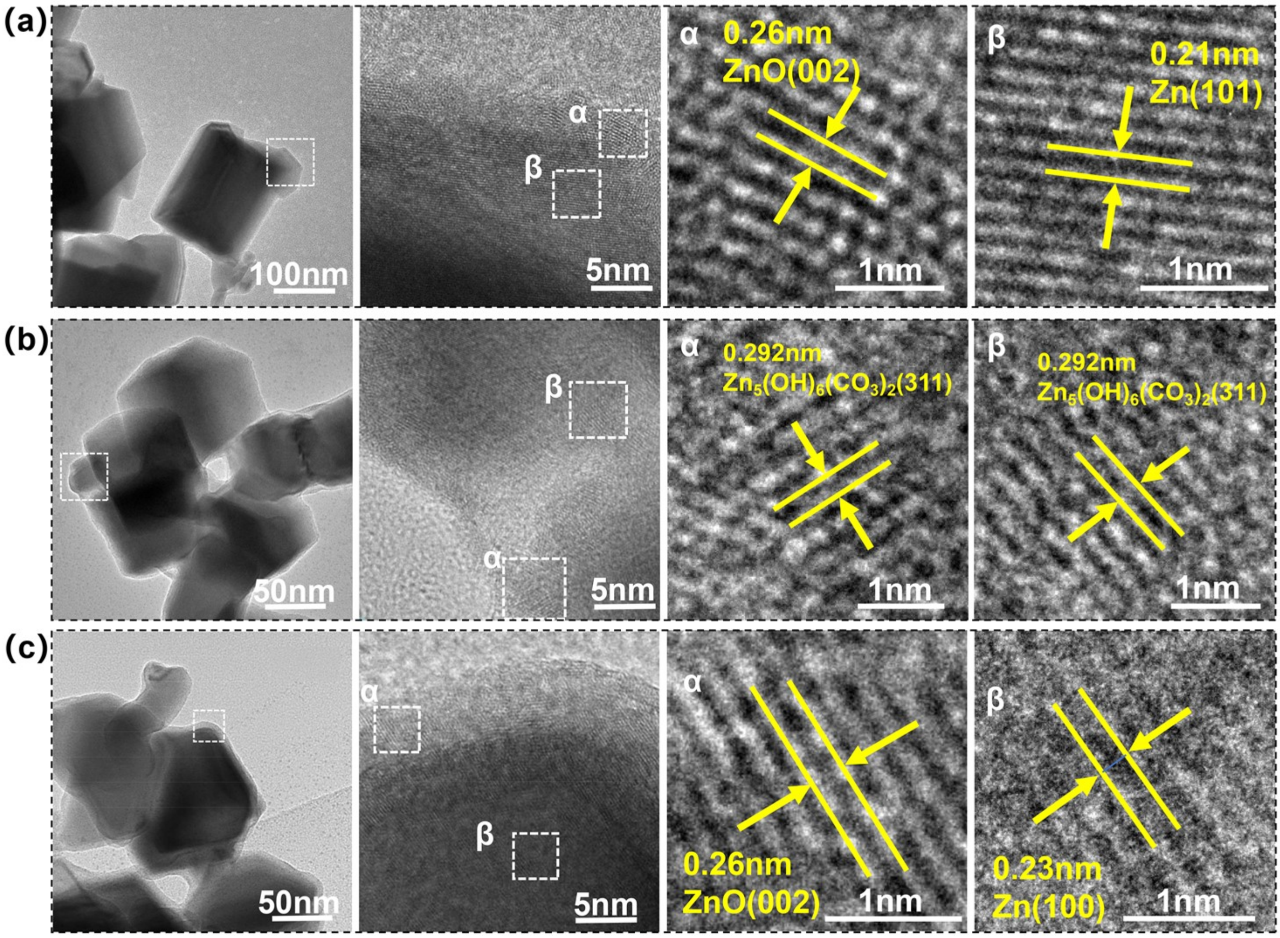

Figure S11. (a) (HR)TEM images of Zn@ZnO-200 at the regions for Zn-ZnO interface; (b) (HR)TEM images of Zn@ZnO-200 at the regions for undecomposed $Zn_5(OH)_6(CO_3)_2$; (c) (HR)TEM images of Zn@ZnO-800 with obvious Zn-ZnO interfacial structure.

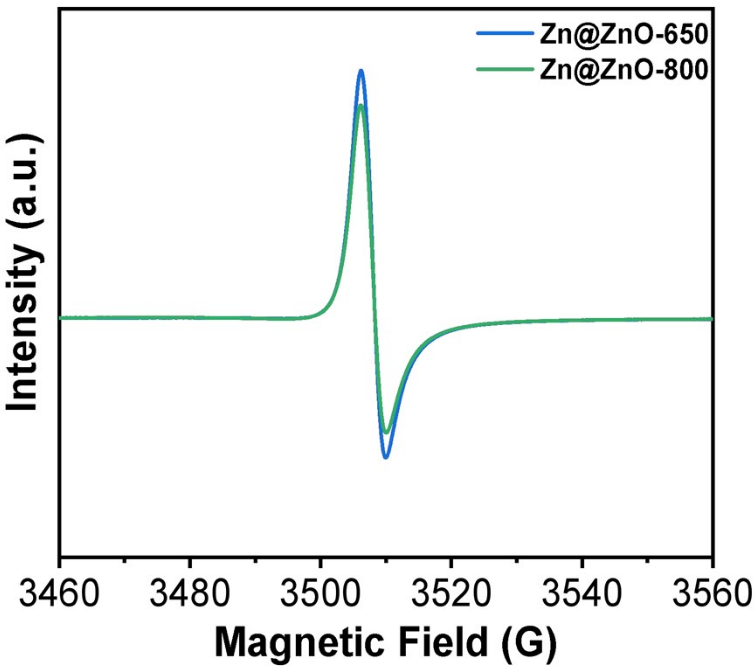

Figure S12. EPR results for Zn@ZnO-650 and Zn@ZnO-800.

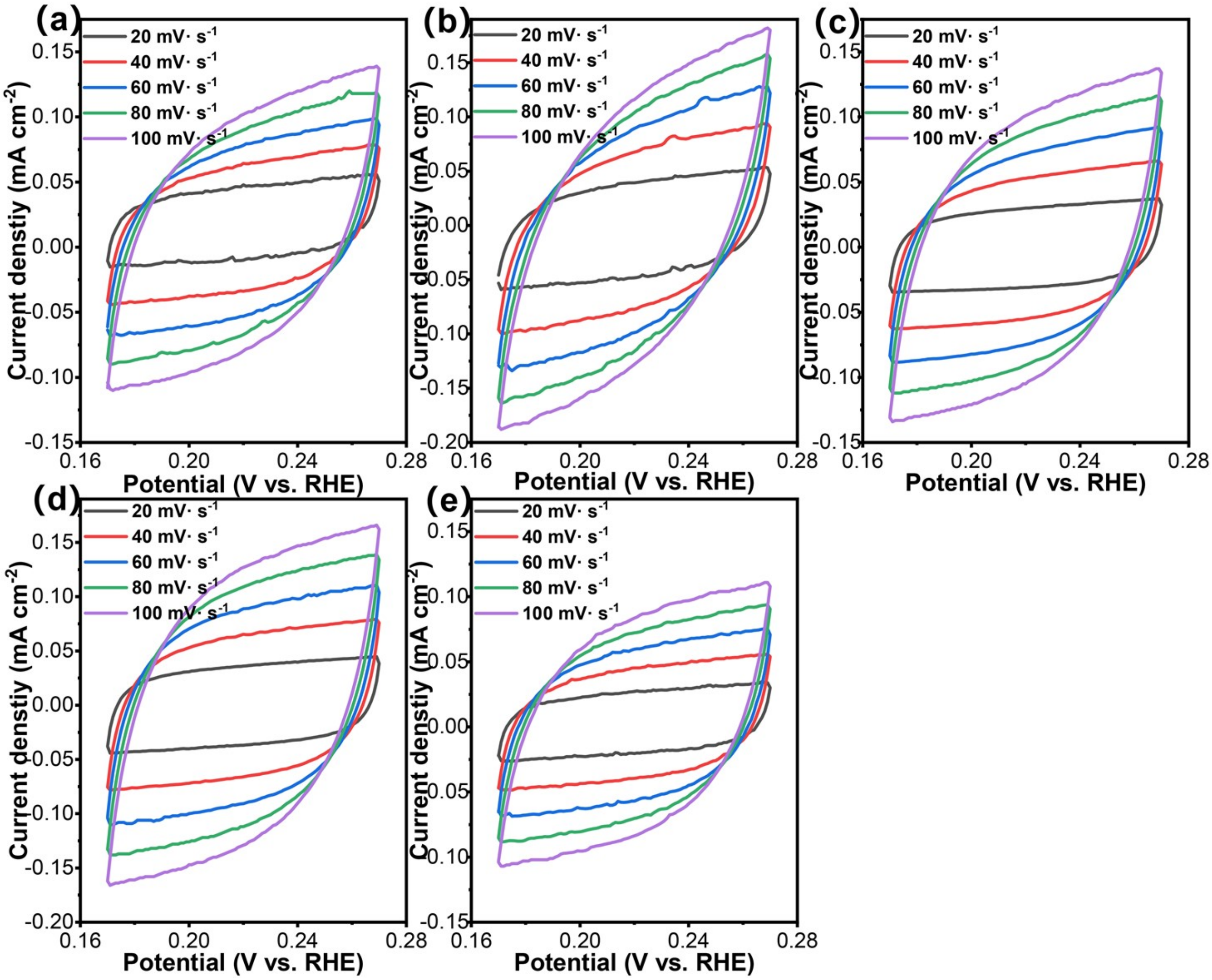

Figure S13. Cyclic voltammograms curves were performed at various scan rates (20, 40, 60, 80, and 100 mV·s^{-1}) on (a) Zn@ZnO-200; (b) Zn@ZnO-350; (c) Zn@ZnO-500; (d) Zn@ZnO-650 and (e) Zn@ZnO-800 in a non-Faraday region of 0.17−0.27 V (*vs.* RHE) in CO_2-saturated 0.1 M $KHCO_3$.

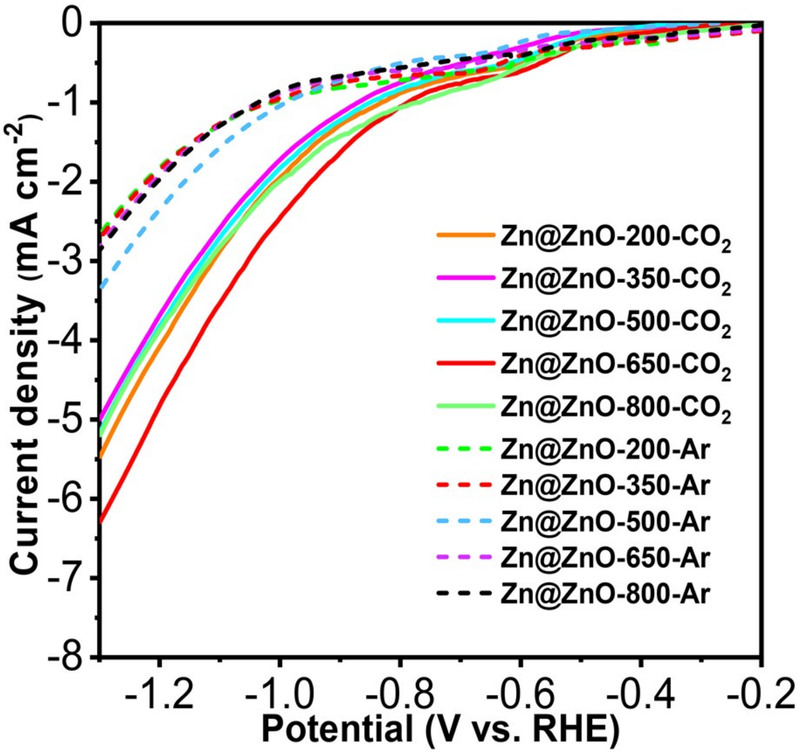

Figure S14. LSV curves of Zn@ZnO-*T* in CO_2- and Ar-saturated 0.1 M $KHCO_3$.

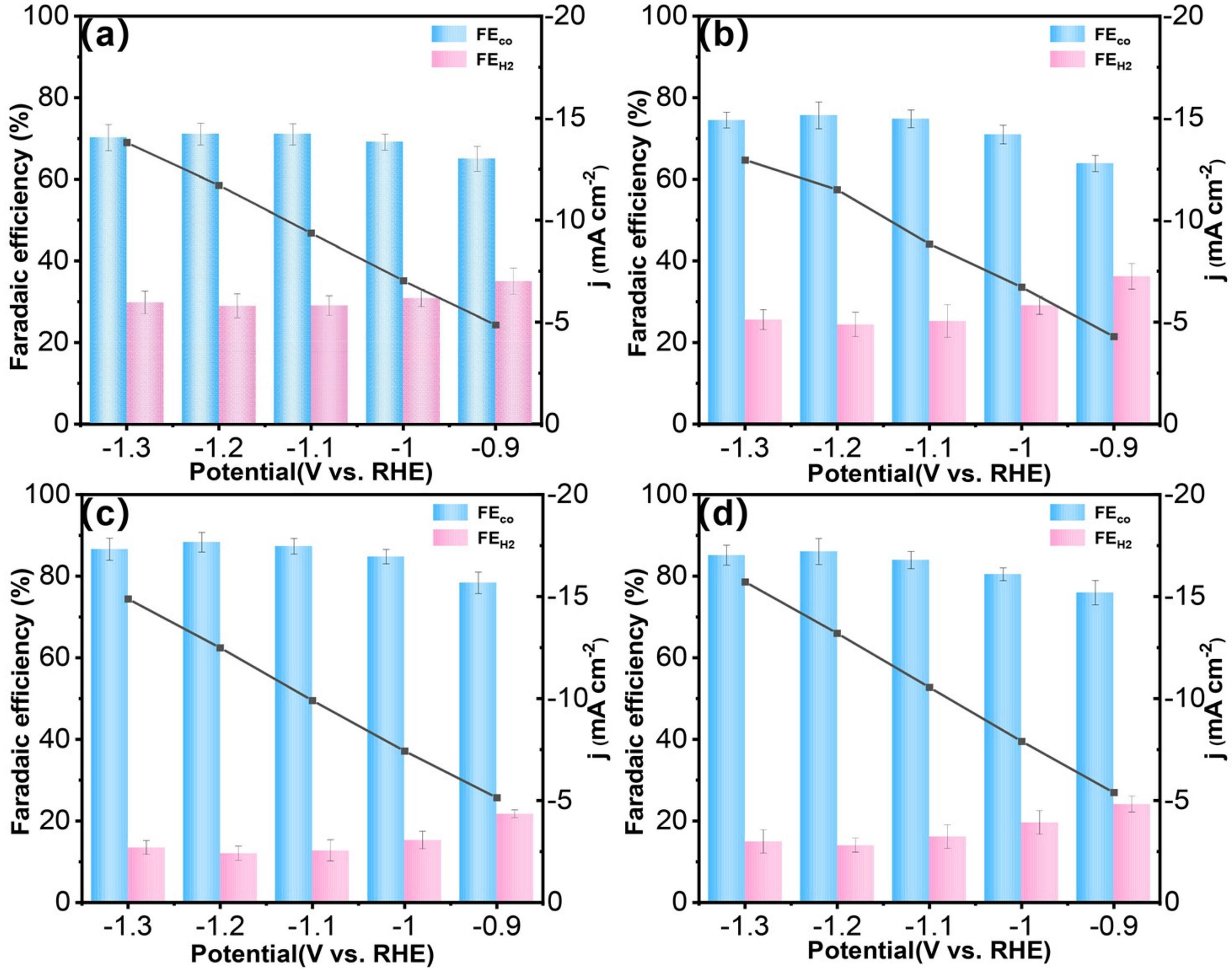

Figure S15. FEs for different products and current density at different potentials for (a) Zn@ZnO-200; (b) Zn@ZnO-350; (c) Zn@ZnO-500; (d) Zn@ZnO-800.

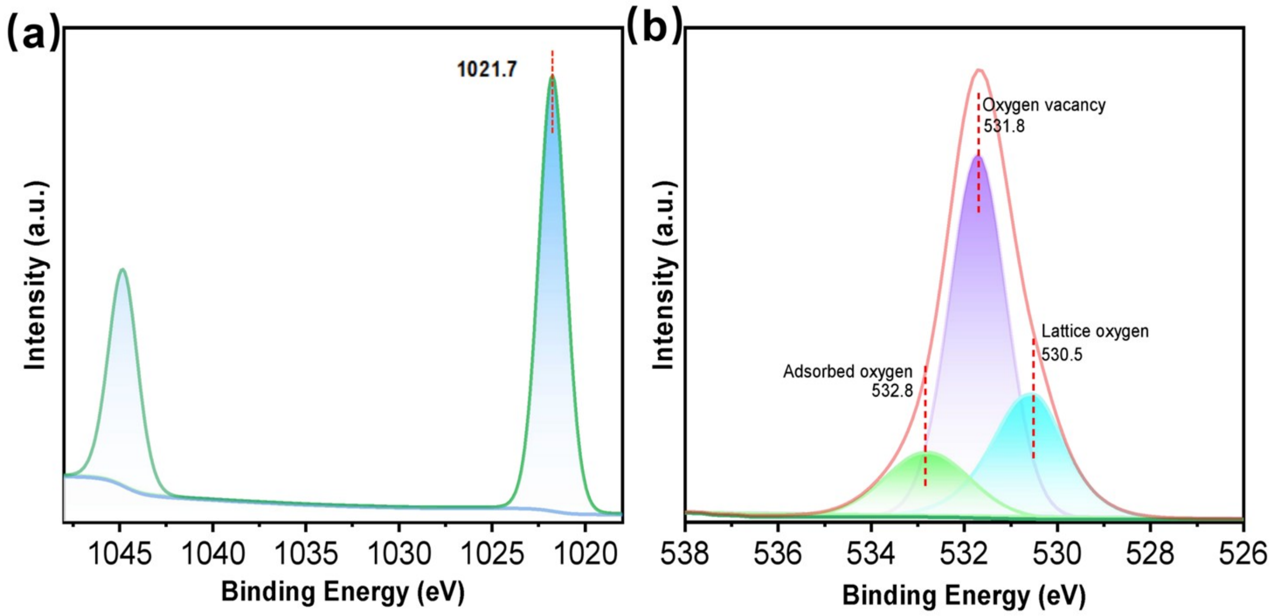

Figure S16. XPS spectra of Zn@ZnO-650 after long-term test for 16 h: (a) Zn 2p; (b) O 1s.

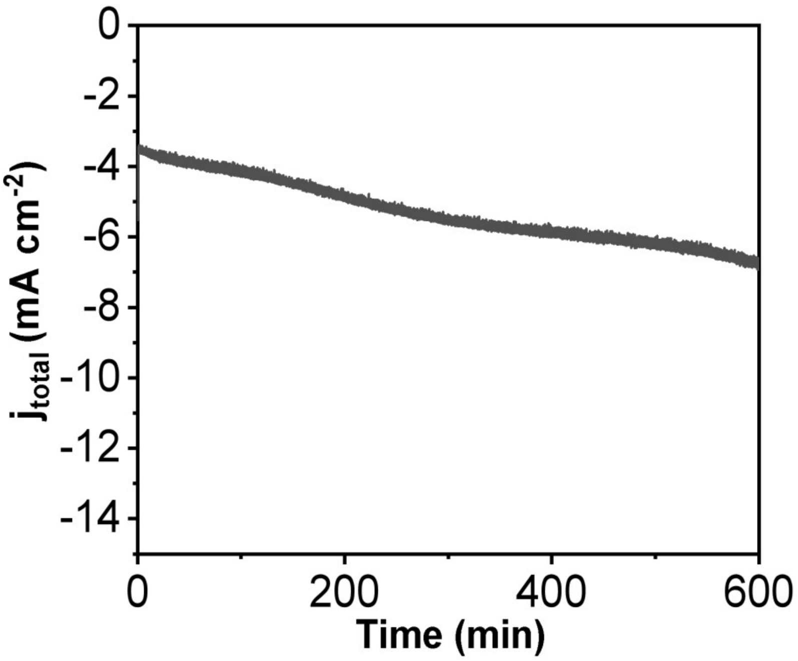

Figure S17. Long-term test of carbon paper electrode without Zn@ZnO-650 catalyst at −1.2 V (*vs.* RHE).

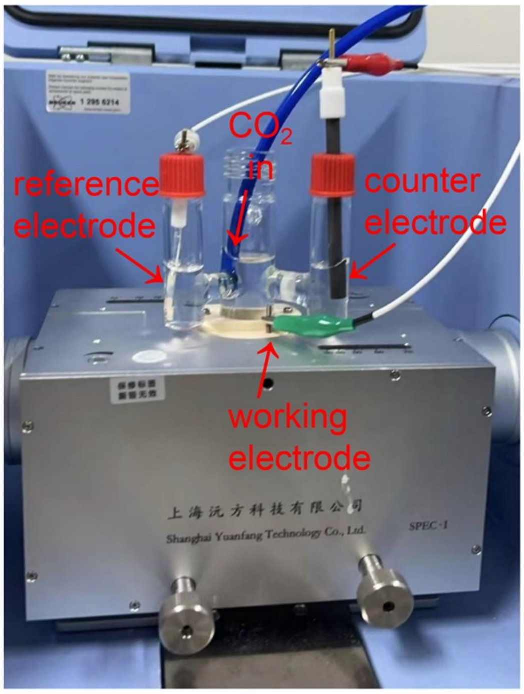

Figure S18. The in situ ATR-SEIRAS testing device.

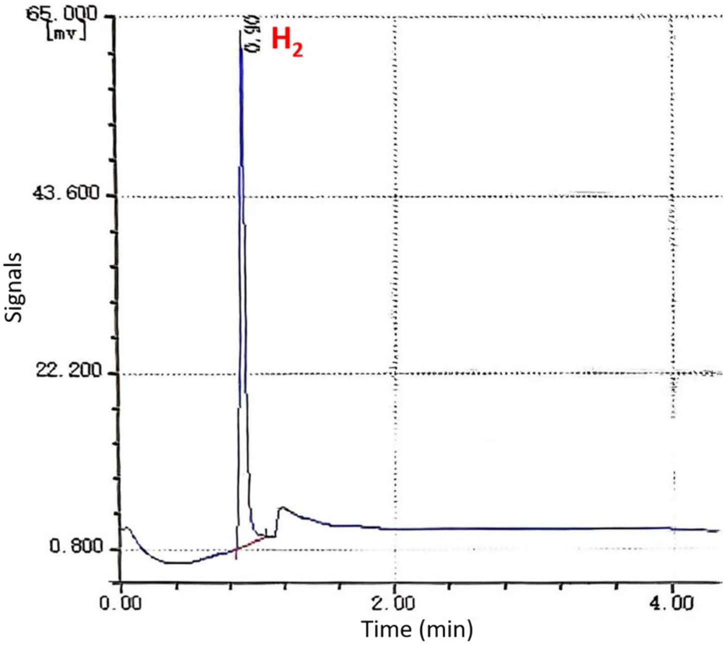

Figure S19. Signal of hydrogen in gas chromatography.

We calculated the hourly hydrogen mass production of Zn@ZnO-650 and Zn@ZnO-200 based on the experimental data from gas chromatography using the following formula:

$$m = C_i \cdot v \cdot \mathrm{M} \cdot V_\mathrm{m}^{-1} \cdot \mathrm{t}^{-1}$$

where m represents the mass production of the target gas, with the unit of $\mathrm{g \cdot h^{-1}}$; C_i is the volume concentration of the target gas calculated from the peak area obtained by the gas chromatograph, with the unit of ppm; v refers to the gas flow rate, usually in the unit of $\mathrm{m^3 \cdot h^{-1}}$; M is the molar mass of the target gas, with the unit of $\mathrm{g \cdot mol^{-1}}$; Vm is the molar volume of the gas, which is taken as 0.0224 $\mathrm{m^3 \cdot mol^{-1}}$ at standard temperature and pressure; t is the reaction time, with the unit of h. The calculation results show that at −1.2 V vs. RHE, the mass production of H_2 on Zn@ZnO-200 is 5.78×10^{-5} $\mathrm{g \cdot h^{-1}}$, and that on Zn@ZnO-650 is 3.76×10^{-5} $\mathrm{g \cdot h^{-1}}$. Thus, the abundant Zn-ZnO interface with oxygen vacancies in Zn@ZnO-650 can effectively inhibit the occurrence of HER.

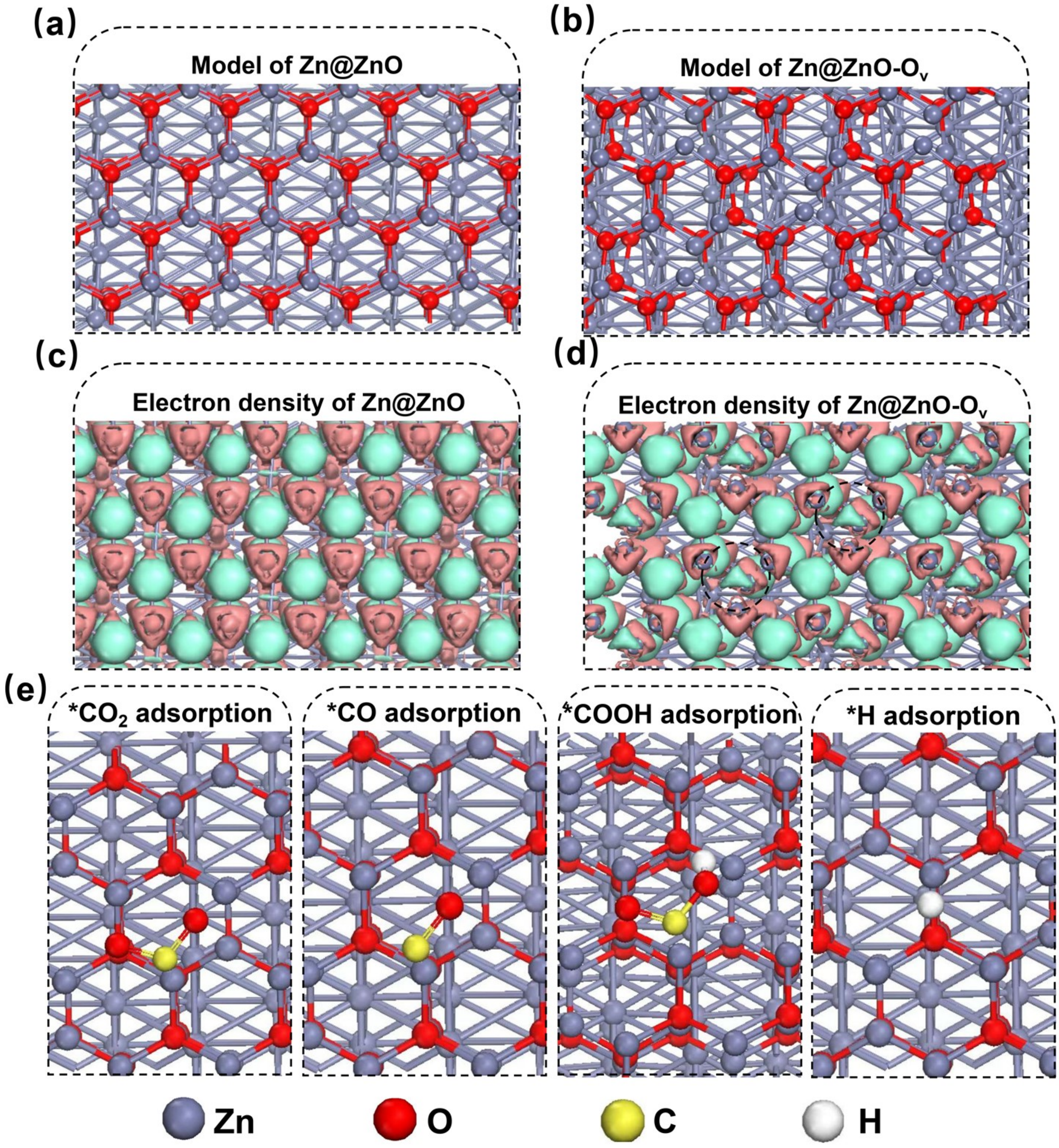

Figure S20. Models of (a) Zn@ZnO with Zn-ZnO interface and (b) Zn@ZnO-O$_v$ with abundant oxygen vacancies in ZnO layer. Electron density of (c) Zn@ZnO with Zn-ZnO interface and (d) Zn@ZnO-Ov with abundant oxygen vacancies in ZnO layer. The dashed area indicates the oxygen vacancies. (e) Models of different species ($^*CO_2$, $^*CO$, $^*COOH$ and $^*H$) adsorbed on Zn@ZnO-O$_v$ surface.

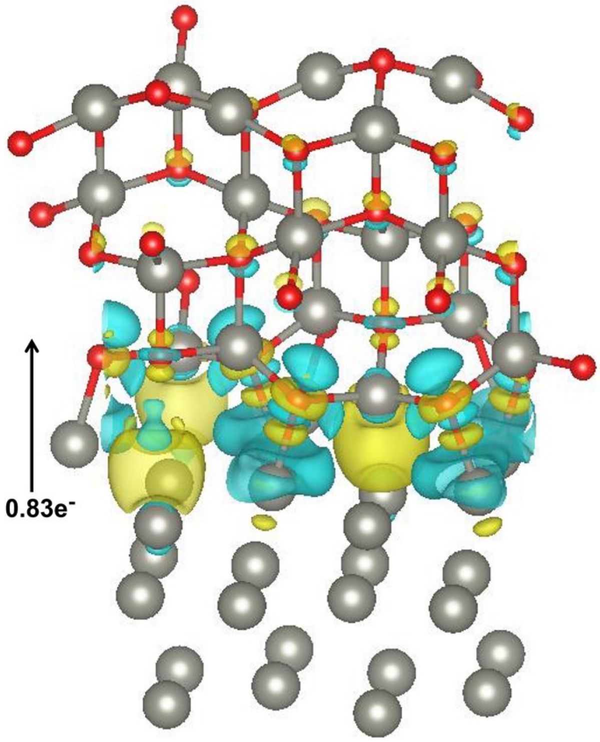

Figure S21. Differential electron densities of Zn and ZnO layers.

Table S1. Fitted EXAFS results for ZnO-650 and Zn@ZnO-650 with different pre-treatment time with Zn and ZnO as reference standards.

Sample [a]	**Path**	***N***[b]	***R***[c]**/Å**	**σ^2/Å^2** [d]
ZnO-650（0min）	Zn−O	3.33	1.96	0.003
Zn@ZnO-650（10min）	Zn−O	2.40	1.97	0.005
	Zn−Zn	0.80	2.66	0.004
	Zn−O−Zn	10.7	3.24	0.014
Zn@ZnO-650（20min）	Zn−O	1.97	1.96	0.007
	Zn−Zn	2.12	2.66	0.010
	Zn−O−Zn	4.45	3.21	0.012
Zn@ZnO-650（40min）	Zn−O	1.10	1.96	0.006
	Zn−Zn	5.50	2.67	0.009

[a] S_o^2 was fixed as 0.95. ΔE_0 was refined as a global fit parameter, all within ± 10 eV. Data ranges: $3.0 \leq k \leq 11.0$ Å^{-1}, $1.0 \leq R \leq 3.0$ Å. The numbers of variable parameters are 7, 10, 10 and 7, out of a total of 11.1, 9.8, 9.8 and 9.8 independent data points. R factor are 1.6%, 1.7%, 0.2% and 3.5% respectively. [b] CN is the coordination number. [c] R is the distance between absorbent and backscatter atoms. [d] σ^2 is the Debye-Waller factor.

Table S2. Performances of Zn-based catalysts in CO_2RR.

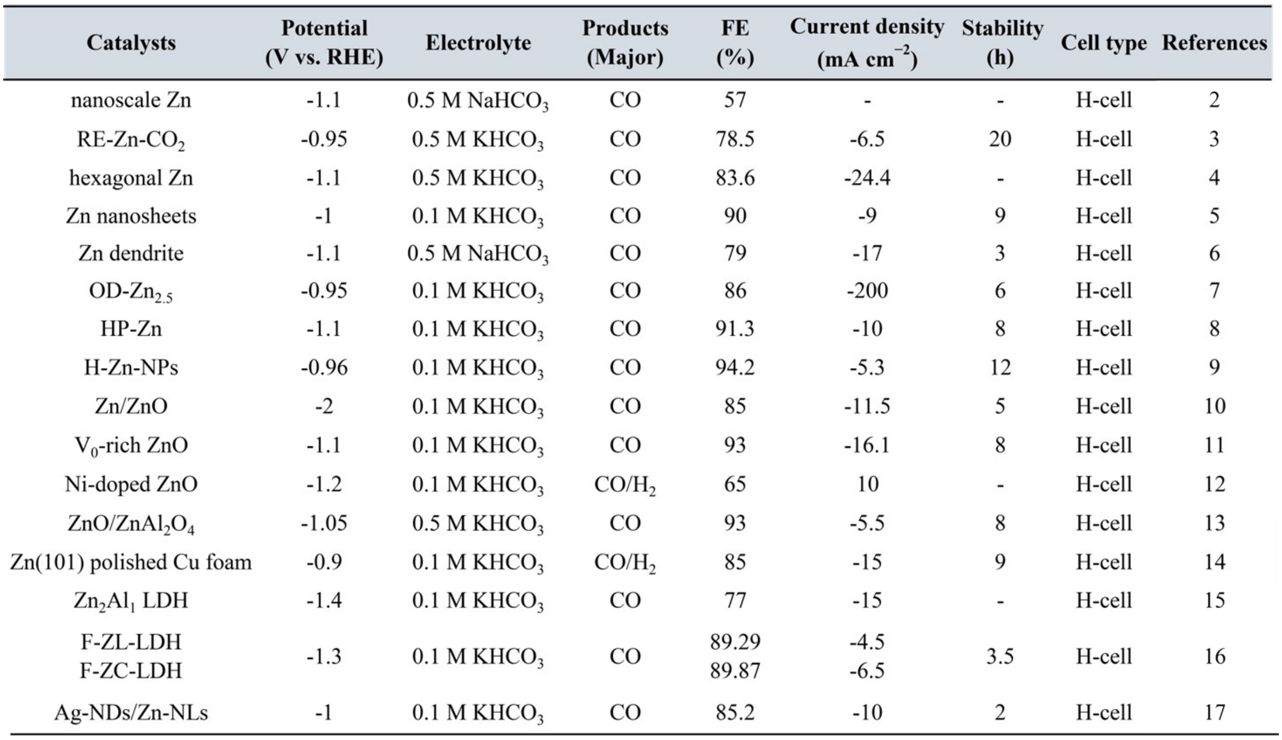

Catalysts	Potential (V vs. RHE)	Electrolyte	Products (Major)	FE (%)	Current density (mA cm^{-2})	Stability (h)	Cell type	References
nanoscale Zn	-1.1	0.5 M $NaHCO_3$	CO	57	-	-	H-cell	2
RE-Zn-CO_2	-0.95	0.5 M $KHCO_3$	CO	78.5	-6.5	20	H-cell	3
hexagonal Zn	-1.1	0.5 M $KHCO_3$	CO	83.6	-24.4	-	H-cell	4
Zn nanosheets	-1	0.1 M $KHCO_3$	CO	90	-9	9	H-cell	5
Zn dendrite	-1.1	0.5 M $NaHCO_3$	CO	79	-17	3	H-cell	6
OD-$Zn_{2.5}$	-0.95	0.1 M $KHCO_3$	CO	86	-200	6	H-cell	7
HP-Zn	-1.1	0.1 M $KHCO_3$	CO	91.3	-10	8	H-cell	8
H-Zn-NPs	-0.96	0.1 M $KHCO_3$	CO	94.2	-5.3	12	H-cell	9
Zn/ZnO	-2	0.1 M $KHCO_3$	CO	85	-11.5	5	H-cell	10
V_0-rich ZnO	-1.1	0.1 M $KHCO_3$	CO	93	-16.1	8	H-cell	11
Ni-doped ZnO	-1.2	0.1 M $KHCO_3$	CO/H_2	65	10	-	H-cell	12
ZnO/$ZnAl_2O_4$	-1.05	0.5 M $KHCO_3$	CO	93	-5.5	8	H-cell	13
Zn(101) polished Cu foam	-0.9	0.1 M $KHCO_3$	CO/H_2	85	-15	9	H-cell	14
Zn_2Al_1 LDH	-1.4	0.1 M $KHCO_3$	CO	77	-15	-	H-cell	15
F-ZL-LDH F-ZC-LDH	-1.3	0.1 M $KHCO_3$	CO	89.29 89.87	-4.5 -6.5	3.5	H-cell	16
Ag-NDs/Zn-NLs	-1	0.1 M $KHCO_3$	CO	85.2	-10	2	H-cell	17

Table S3. Electron transfer based on analysis of Bader charge calculations.

Function interface	**Transferred electrons**
Zn→ZnO	+0.83e-
Zn→ZnO-O_v	+0.93e-
Zn@ZnO→CO_2	+0.84e-
Zn@ZnO-O_v→CO_2	+1.29e-

References

1 S. Mu, H. Lu, Q. Wu, L. Li, R. Zhao, C. Long and C. Cui, *Nat. Commun.* **2022**, 13, 3694.

2 F. J. Quan, D. Zhong, H. C. Song, F. L. Jia and L. Z. Zhang, *J. Mater. Chem. A* **2015**, 3, 16409-16413.

3 D. L. T. Nguyen, M. S. Jee, D. H. Won, H. Jung, H. S. Oh, B. K. Min and Y. J. Hwang, *ACS Sustain. Chem. Eng.* **2017**, 5, 11377-11386.

4 D. H. Won, H. Shin, J. Koh, J. Chung, H. S. Lee, H. Kim and S. I. Woo, *Angew. Chem. Int. Ed.* **2016**, 55, 9297-9300.

5 K. H. Liu, J. Z. Wang, M. M. Shi, J. M. Yan and Q. Jiang, *Adv. Energy Mater.* **2019**, 9, 1900276.

6 J. Rosen, G. S. Hutchings, Q. Lu, R. V. Forest, A. Moore and F. Jiao, *ACS Catal.* **2015**, 5, 4586-4591.

7 M. P. L. Kang, M. J. Kolb, F. Calle-Vallejo and B. S. Yeo, *Adv. Funct. Mater.* **2022**, 32, 2111597.

8 W. Y. Wang, X. H. He, K. Zhang and Y. G. Yao, *Chem. Commun.* **2022**, 58, 5096-5099.

9 J. Xiao, M. R. Gao, S. B. Liu and J. L. Luo, *ACS Appl. Mater. Interfaces* **2020**, 12, 31431-31438.

10 Q. Xiang, F. Li, J. L. Wang, W. L. Chen, Q. S. Miao, Q. F. Zhang, P. Tao, C. Y. Song, W. Shang, H. Zhu, T. Deng and J. B. Wu, *ACS Appl. Mater. Interfaces* **2021**, 13, 10837-10844.

11 Z. G. Geng, X. D. Kong, W. W. Chen, H. Y. Su, Y. Liu, F. Cai, G. X. Wang and J. Zeng, *Angew. Chem. Int. Ed.* **2018**, 57, 6054-6059.

12 J. L. Wang, Q. Xiang, W. C. Zhang, F. L. Shi, F. Li, P. Tao, C. Y. Song, W. Shang, T. Deng and J. B. Wu, *ACS Appl. Energ. Mater.* **2022**, 5, 5531-5539.

13 L. Wang, Y. Gao, S. X. Yu, Y. Sun, Z. Yuan, Y. F. Liang and L. Li, *Catal. Lett.* **2024**, 154, 4032-4043.

14 B. H. Qin, Y. H. Li, H. Q. Fu, H. J. Wang, S. Z. Chen, Z. L. Liu and F. Peng, *ACS Appl. Mater. Interfaces* **2018**, 10, 20530-20539.

15 N. Yamaguchi, R. Nakazato, K. Matsumoto, M. Kakesu, N. C. Rosero-Navarro and A. Miura, K. Tadanaga, *J. Asian Ceram. Soc.* **2023**, 11 ,406-411.

16 J. Y. Wang, T. X. Liu, R. S. Xu and Y. P. Zhang, *Catal. Lett.* **2024**, 154, 2687-2700.

17 S. Y. Yang, M. H. Jiang, M. Wang, L. Wang, X. M. Song, Y. D. Wang, Z. X. Tie and Z. Jin, *Nano Res.* **2023**, 16, 8910-8918.